Dynamics of Air Drawing in the Melt Blowing of Nonwovens from Isotactic Polypropylene by Computer Modeling

Leszek Jarecki,[1] Andrzej Ziabicki,[1] Zbigniew Lewandowski,[2] Anna Blim[1]

[1]*Institute of Fundamental Technological Research, Polish Academy of Sciences, Pawinskiego 5B, 02-106 Warsaw, Poland*
[2]*University of Bielsko-Biala, Institute of Textile Engineering and Polymer Materials, Willowa 2, 43-309 Bielsko-Biala, Poland*

Received 5 March 2009; accepted 13 December 2009
DOI 10.1002/app.31973
Published online 20 July 2010 in Wiley Online Library (wileyonlinelibrary.com).

ABSTRACT: The dynamics of stationary air drawing in the melt blowing of nonwovens were determined on the basis of a single-filament model in a thin-filament approximation that accounts for polymer viscoelasticity, heat of viscous friction in the polymer bulk, and surface energy. Predetermined distributions of the air velocity and temperature along the melt blowing axis were assumed. Axial profiles of the polymer velocity, temperature, elongation rate, filament diameter, tensile stress, and extrapressure were computed for the melt blowing of isotactic polypropylene. The effects of the air-jet velocity, die-to-collector distance, and polymer molecular weight are discussed. We predicted that the filament attenuation and velocity at the collector located in the air-drawing zone would increase with increasing die-to-collector distance. The air-drawing zone was shorter for higher air velocities and lower molecular weights. No online crystallization was predicted before the achievement of the collector, and melt bonding of the filament in the web should have occurred during cooling on the collector, accompanied by spherulitic crystallization. Significant online extrapressure in the filament was predicted in the case of supersonic air jets as resulting from polymer viscoelasticity, which could have led to longitudinal splitting of the polymer into subfilaments. © 2010 Wiley Periodicals, Inc. J Appl Polym Sci 119: 53–65, 2011

Key words: fibers; melt; modeling; poly(propylene) (PP); processing

INTRODUCTION

Melt blowing is a rapid technology of nonwoven production from a variety of thermoplastic polymers, in which a web structure is obtained in a one-step process from the melt by the application of high-velocity, hot-air jets.[1,2] In the process, two convergent air jets blown from a dual-slot die attenuate the melt streams extruded from a single row of orifices. Intensive experimental studies in recent years on the multivariable process and its products have resulted in a considerable improvement of the technique and the properties of the nonwovens.[3–8] Important properties of the nonwovens associated with the surface activity of the fibers strongly improve with a reduction in the fiber diameter. The diameter of the web fibers melt-blown from polypropylene and other thermoplastics has been reported in a wide range, between 70 and 1.6 μm, in the literature.[3,5] Experimental investigations have indicated that thinner fibers are obtained at faster air jets, higher melt temperatures, lower mass outputs (W's) of the polymer, and longer die-to-collector distances (L's).[5,6,8] The process dynamics and web structure are also influenced by the rheological properties of the melt associated with the polymer molecular weight and by the geometry of the air die assembly.

The majority of the filament attenuation is caused by air drawing and occurs within a short range of the process axis adjacent to the spinneret, where individual filaments are aligned to the air-jet axis and remain unentangled. The air-drawing forces spin the filaments with an elongation rate (dV/dz) much higher than that used in classical melt spinning. Some attenuation beyond the air-drawing zone has also been reported as caused by interfilament collisions and entanglements.[3,7]

The role of the processing and material parameters in melt blowing has been the subject of many experimental investigations in the last decade, but literature on the modeling and computer simulation of process dynamics is scarce. To overcome difficulties in the modeling, a surface-response methodology was adopted in the study in ref. 5 to develop and optimize the process. However, the method is based on time-consuming experimental measurements in a wide range of high numbers of the

Correspondence to: L. Jarecki (ljarecki@ippt.gov.pl).

process parameters. An attempt to predict the air-drawing effects by computer modeling has been presented[9,10] with the application of classical equations of melt spinning for the case of the melt blowing of polypropylene. The diameter of the fibers predicted in the computations was rather high, above 50 μm. The model did not account for the melt viscoelasticity, heat of viscous friction in the polymer bulk, and filament surface energy, effects that could contribute to the process dynamics under high-velocity air jets attenuating the filaments to a few micrometers.

MODEL ASSUMPTIONS

In the melt blowing of nonwovens, the polymer melt is usually extruded from a single row of orifices evenly distributed along the spinning beam. We considered the attenuation of polymer streams in the air-drawing zone, where the influence of interfilament contacts and entanglements could be neglected. In the zone, the air velocity [$V_a(z)$] dominates velocity of the polymer streams, and attenuation of the filaments occurs under high air-drag forces. The air-drawing zone extends between the spinneret and a point on the process axis where the velocities of the filament and the air approach each other and the drawing potential of the air jets decreases to zero. Consequently, the velocity of the filaments attains a maximum; this is followed by a monotonic decrease, which causes interfilament collisions, intensive coiling, and entanglements.[7]

To discuss the process dynamics, we use predetermined air fields and the equations of melt spinning in a single-filament approximation. Fundamental equations of melt spinning were proposed in refs. 11–14 and have been developed by other authors.[15–17] In this article, we use a single-, thin-filament model of melt spinning[17,18] that accounts for the nonlinear viscoelasticity, heat of viscous friction in the polymer bulk, and filament surface tension [$\gamma(z)$]. The influence of viscous friction and surface tension, usually neglected in melt spinning, is analyzed because, in pneumatic processes, very high dV/dz values are introduced, which attenuate the filaments very quickly within a very short range of the process axis. The computations focus on the role of the air-jet velocity, L, and polymer molecular weight [melt flow rate (MFR)] on the filament attenuation in the air-drawing zone. Distributions of the filament velocity [$V(z)$], filament temperature [$T(z)$], filament tensile stress [$\Delta p(z)$], and filament rheological extrapressure [$p_{rh}(z)$] in the polymer bulk along the melt blowing axis are also discussed. Example computations are shown for the melt blowing of nonwovens from isotactic polypropylene (iPP).

Cartesian coordinates, with the origin at the spinneret, the x axis along the spinning beam, and the z axis along the centerline, were chosen. The geometry of the process allowed us to reduce the model to two dimensions in the (y,z) plane normal to the curtain of the blown filaments. The plain showed a symmetry axis along the centerline of the air jets. A high length-to-width ratio of the die assembly, exceeding 50, as recommended in ref. 19, allowed us to neglect the end effects. The single-, thin-filament approximation widely used in the modeling of melt spinning reduced the problem to one variable: the axial distance (z).

Axial profiles of $V(z)$, $T(z)$, $\Delta p(z)$, and $p_{rh}(z)$ were considered as the values averaged over the radial cross section of the filament at point z. The air conditions were approximated by $V_a(z)$, air temperature [$T_a(z)$], and air pressure [$p_a(z)$] distributions along the z axis, determined in the form of continuous analytical functions in the absence of the filament. The validity of the approximation by predetermined air fields was proven experimentally for melt blowing in the study in ref. 20. We used the air fields computed for jets blown at different initial air velocities (V_{a0}'s) from the die slots shown in Figure 1.[21,22]

MODEL EQUATIONS

Experimental observations[7] indicated that intensive air drawing of the polymer melt takes place within a range of the z axis where $V_a(z)$ much exceeds $V(z)$. The range is limited by the point on the z axis at which the $V_a(z)$ and $V(z)$ values approach each other. The mass conservation, force balance, and energy conservation equations for the filament in the air-drawing zone read as follows:

$$\rho(z)V(z)\frac{\pi D^2(z)}{4} = W \tag{1}$$

$$\frac{dF}{dz} = W\frac{dV}{dz} + \pi D(z)p_{zr}(z) - \frac{\pi D^2(z)}{4}\rho(z)g - \frac{\pi}{2}\frac{d}{dz}[\gamma(z)D(z)] \tag{2}$$

where dF/dz is axial gradient of the tensile force, d/dz denotes the axial gradient operator, and the z axis is vertical.

$$\rho(z)C_p(z)V(z)\frac{dT}{dz} = -\frac{4\alpha^*(z)}{D(z)}[T(z) - T_a(z)] + tr[\mathbf{p}(z)\times\dot{\mathbf{e}}(z)] \tag{3}$$

where dT/dz is axial gradiant of the filament temperature, tr denotes the trace operator, $\mathbf{p}(z)$ is local stress tensor, $\dot{\mathbf{e}}(z)$ is local elongation rate tensor, the z axis is vertical, $D(z)$ is the local diameter of the filament at a constant W, $\rho(z)$ is the local polymer density, $p_{zr}(z)$ is the air friction shear stress on the filament surface, g is the acceleration of gravity,

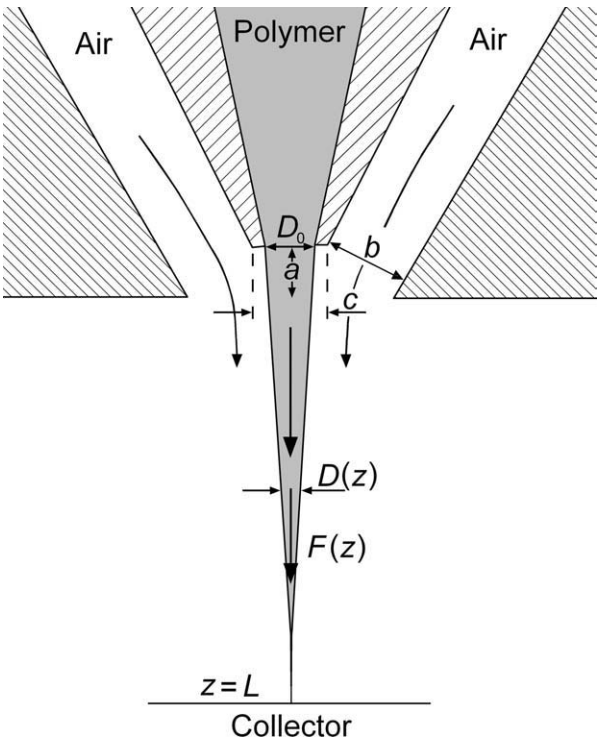

Figure 1 Geometry of the die assembly used in the simulation of the air fields:[21] a (=0.3 mm) is the recess of the nosepiece, b (=0.5 mm) is the width of the air slots, c (= 0.5 mm) is the width of the spinneret, and D_0 (=0.35 mm) is the diameter of the spinneret orifice. The inclination of the air slots to the z axis was 28.25°. $z = L$ is the collector location in the air-drawing zone.

$C_p(z)$ is the specific heat of the polymer, and α^* is the heat-exchange coefficient.

The last terms in eqs. (2) and (3) account for $\gamma(z)$ and the friction heat generated in the polymer bulk,[14,17] respectively. The $\gamma(z)$ in eq. (2) is nearly proportional to local filament attenuation (dD/dz). The attenuation is extremely rapid at high-velocity air jets and exceeds by an order of magnitude the values reported in melt spinning.[7] Experimental observations[3,7] indicated a reduction in $D(z)$ to 10% of its initial value over a distance range less than 2 cm from the die. The volume density of the viscous friction heat, expressed by the product of $\Delta p(z)$ and dV/dz, is calculated as follows:[17]

$$tr[\mathbf{p}(z) \times \dot{\mathbf{e}}(z)] = \Delta p(z) dV/dz$$

The mass conservation equation of stationary melt spinning is valid under the condition of dominating $V_a(z)$ [$V_a(z) > V(z)$]. Equation (1) loses its validity beyond the air-drawing zone, where $V(z)$ monotonically decreases after it approaches a maximum at the zone edge, but a slight decrease in the diameter is still observed.[7] The force balance eq. (2) accounts for inertia, air friction, gravity, and surface tension.

The energy balance eq. (3) accounts for convective heat exchange between the filament and the air caused by the local difference in the temperature [$T(z) - T_a(z)$]. α^* is determined from the correlation between the Nusselt number (Nu) and Reynolds number (Re; $\mathrm{Nu} = 0.42\mathrm{Re}^{0.334}$), confirmed by Bansal and Shambaugh[3] for the melt blowing of polypropylene nonwovens.

Crystallization heat effects were omitted, as they are absent under usual melt blowing conditions. As reported in the literature,[7] the filaments of iPP do not crystallize during melt blowing until they reach the collector. No oriented crystallization was predicted by the computation performed for the process with the collector located at a fixed distance of 20 cm from the spinneret.[23,24]

$p_{zr}(z)$ is calculated as follows:

$$p_{zr}(z) = \frac{1}{2} C_f(z) \rho_a(z) [V(z) - V_a(z)]^2 \mathrm{sgn}[V(z) - V_a(z)] \tag{4}$$

where $C_f(z)$ is the air friction coefficient and $\rho_a(z)$ is the local air density. $p_{zr}(z)$ depends on the local difference between $V(z)$ and $V_a(z)$ [$V(z) - V_a(z)$] and is negative in the entire air-drawing zone. $C_f(z)$ is calculated as follows:[25]

$$C_f(z) = \beta \left\{ \frac{D(z)|V(z) - V_a(z)|}{\nu_a(z)} \right\}^{\alpha} \tag{5}$$

where β and α are experimental correlation constants and $\nu_a(z)$ is the kinematic viscosity of the air. For melt blowing, we assume $\beta = 0.78$ and $\alpha = -0.61$.[26] $\nu_a(z)$ depends on the local $T_a(z)$ and reads (at atmospheric pressure) as follows:[17]

$$\nu_a(z) = 4.1618 \times 10^{-9} \frac{T_a^{5/2}(z)}{T_a(z) + 114} (\mathrm{m}^2/\mathrm{s}) \tag{6}$$

The thermal conductivity of the air, λ_a which affects α^* in eq. (3) ($\alpha^* = 0.42 \lambda_a \nu_a^{-0.334} D^{0.666} (V - V_a)^{0.334}$, from the relation between Nu and Re[3]) is approximated by the conductivity of dry air [$\lambda_a(z)$] at atmospheric pressure:[17]

$$\lambda_a(z) = 2.0848 \times 10^{-3} \frac{T_a^{3/2}(z)}{T_a(z) + 114} (\mathrm{J\,m^{-1}s^{-1}K^{-1}}) \tag{7}$$

The following dependences of the melt $\rho(z)$, $\gamma(z)$, and $C_p(z)$ on the temperature were chosen for iPP[27,28]

$$\rho(z) = \frac{10^3}{1.145 + 9.03 \times 10^{-4}[T(z) - 273]} \quad (\mathrm{kg/m^3}) \tag{8}$$

$$\gamma(z) = 2.94 \times 10^{-2} - 5.6 \times 10^{-5} [T(z) - 296] \quad (\mathrm{N/m}) \tag{9}$$

$$C_p(z) = C_{p0} + C_{p1}\,[T(z) - 273] \tag{10}$$

where $C_{p0} = 1.5358 \times 10^3$ J kg^{-1} K^{-1} and $C_{p1} = 10.13$ J kg^{-1} K^{-2} are experiment constants.

The Phan-Thien/Tanner constitutive equation of viscoelasticity was assumed as follows:[29,30]

$$\tau \exp\left(-\varepsilon \frac{\tau}{\eta} tr\,\boldsymbol{\sigma}\right)[\dot{\boldsymbol{\sigma}} - (1-\xi)2\boldsymbol{\sigma}\dot{\boldsymbol{e}}] + \sigma = 2\eta \exp\left(-\varepsilon \frac{\tau}{\eta} tr\,\boldsymbol{\sigma}\right)\dot{\mathbf{e}} \tag{11}$$

where τ is the relaxation time of the polymer, η is the zero-shear melt viscosity of the polymer, $\boldsymbol{\sigma}$ is the extrastress tensor, $\boldsymbol{\sigma}$ is the time-derivative of the extrastress tensor, and ε and ξ are constants responsible for nonlinear and shear-thinning effects, respectively. For iPP, $\varepsilon = 0.015$ and $\xi = 0.6$.[31] The components of $\boldsymbol{\sigma}$ can be expressed by the tensile stress ($\Delta p = \sigma_{zz} - \sigma_{rr}$, where σ_{zz} and σ_{rr} are axial and radial components of the stress tensor, respectively) and the rheological extrapressure [$p_{rh} = -tr\sigma/3 = -(\sigma_{zz} + 2\sigma_{rr})/3$], which vanishes for purely viscous flow in the limit of zero dV/dz ($\tau \to 0$, $\varepsilon = 0$). In the thin-filament approximation, eq. (11) is converted into two scalar equations for the axial profiles of $\Delta p(z)$ and $p_{rh}(z)$:

$$\tau(z)V(z)\frac{d}{dz}\Delta p + \Delta p(z)\,\exp\left[-3\varepsilon\frac{\tau(z)}{\eta(z)}p_{rh}(z)\right] = 3\eta(z)\frac{dV}{dz} + \tau(z)(1-\xi)[\Delta p - 3p_{rh}(z)]\,\frac{dV}{dz} \tag{12}$$

$$\tau(z)V(z)\frac{d}{dz}p_{rh} + p_{rh}(z)\exp\left[-3\varepsilon\frac{\tau(z)}{\eta(z)}p_{rh}(z)\right] = -\frac{2}{3}\tau(z)(1-\xi)\Delta p(z)\frac{dV}{dz} \tag{13}$$

$\Delta p(z)$ is related to the local tensile force [$F(z)$]:[18]

$$\Delta p(z) = \frac{F(z)}{\pi D^2(z)} \tag{14}$$

The Arrhenius-temperature dependence of the melt shear viscosity [$\eta(T)$] is assumed to be above the glass transition:

$$\eta(T) = \begin{cases} \eta_0(M_w)\exp\left(\frac{E_a}{kT}\right) & T > T_g \\ \infty & T \le T_g \end{cases} \tag{15}$$

where η_0 is a material constant, M_w is the weight-average molecular weight, E_a is the activation energy, T_g is the glass-transition temperature, and k is the Boltzmann constant. For iPP, $E_a/k = 5.292 \times 10^3$ K and $T_g = 253$ K.[14,28] For entangled polymer melts, the front factor η_0 (M_w) = Constant $\times$ $M_w^{3.4}$.[32] The shear viscosity of the melt [$\eta(z)$] at $T(z)$ is calculated as follows:

$$\eta(z) = \eta_{\text{ref}}\left(\frac{M_w}{M_{w,\text{ref}}}\right)^{3.4}\exp\left[\frac{E_a}{k}\left(\frac{1}{T(z)} - \frac{1}{T_{\text{ref}}}\right)\right] \tag{16}$$

where η_{ref} is a reference shear viscosity of the polymer at a reference temperature (T_{ref}) and a reference weight-average molecular weight ($M_{w,\text{ref}}$). $\eta_{\text{ref}} = 3000$ Pa s was chosen for iPP at $T_{\text{ref}} = 493$ K and $M_{w,\text{ref}} = 300{,}000$.[32]

The local relaxation time of the melt [$\tau(z)$] is calculated as

$$\tau(z) = \eta(z)/G(z)$$

where $G(z) = BT(z)$ is the modulus of elasticity proportional to the melt temperature and the constant B is proportional to the volume density of the average number of subchains between the entanglements (ν):[30]

$$B = (1-\xi)^2\nu k$$

$\tau(z)$ is expressed by a reference relaxation time (τ_{ref}) of the melt:

$$\tau(z) = \tau_{\text{ref}}\left(\frac{M_w}{M_{w,\text{ref}}}\right)^{3.4}\exp\left[\frac{E_a}{k}\left(\frac{1}{T(z)} - \frac{1}{T_{\text{ref}}}\right)\right]\frac{T_{\text{ref}}}{T(z)} \tag{17}$$

In the computations, we assumed $\tau_{\text{ref}} = 0.035$ s at $T_{\text{ref}} = 493$ K and $M_{w,\text{ref}} = 300{,}000$ for iPP. τ_{ref} was extrapolated from a value of 0.040 s reported for a shear viscosity of 3420 Pa s at 483 K.[31]

The set of four first-order differential equations of melt drawing obtained from eqs. (1)–(3) and eqs. (12)–(14) was solved by the numerical Runge–Kutta integration procedure, which required initial values for polymer $V(z)$, $T(z)$, $F(z)$, and $p_{rh}(z)$. The initial $V(z)$ was controlled by a constant W, $V(z = 0) = 4W/[\pi D_0^2\ \rho\ (T_0)]$, the initial melt $T(z)$ was constant [$T(z = 0) = T_0$], and the initial $p_{rh}(z)$ was zero [$p_{rh}\ (z = 0) = 0$]. The initial $F(z)$ was controlled indirectly by the dynamic conditions at the collector, where the filament deposited freely onto the nonwoven surface. The initial $F(z)$ [$F(z - 0) = F_0$] was adjusted by an inverse method to zero $F(z)$ at the end of the process axis [$F(z - L) = 0$].

AIR-JET CONDITIONS

The air-jet conditions determined the dynamic interactions and heat exchange between the filament and the air along the process axis z. The z axis was identical to the centerline of the air jets. We assumed axial distributions of $V_a(z)$ and $T_a(z)$ predetermined in ref. 21 for several V_{a0}'s between 30 and 300 m/s and the geometry of the die assembly, shown in Figure 1. The initial air temperature (T_{a0}) was fixed to 300°C and was equal to the melt extrusion

temperature. Experimental investigations in the literature indicated that T_{a0} usually applied in the melt blowing of nonwovens negligibly influences the fiber diameter.[6] The influence of T_{a0} is slightly stronger when it is lower than the melt extrusion temperature, and a slight decrease in the fiber diameter was observed with increasing $T_a(z)$.[3,33] A much more important role was attributed to $V_a(z)$. An increase in V_{a0} is frequently used as a method to intensify filament attenuation and reduce its diameter. The V_{a0} values in the simulation[21] covered the ranges of air-jet velocity reported in the literature.[3,5–7]

In the simulation,[21] the air flow fields were computed with the standard $k - \varepsilon$ turbulence model with the aid of the Fluent 6.3 package (Ansys, Inc. Canonsburg, PA). The zero point of the z axis was set at the spinneret face. The air flow space in the (y,z) plane was wide and long enough to represent dynamics of the air jets active in melt blowing. The limits of the air fields in the y and z directions, with the centerline symmetry z axis and the limit $z_{\max} =$ 20 cm, were determined by the experience of other authors.[10,34] In the computation technique, the net grid was concentrated at the proximity of the air slots and did enlarge with increasing distance from the die toward the boundaries of the fields.

In the vicinity of the slots where the spinneret was recessed, there was a negative axial $V_a(z)$, which next inverted its direction and rapidly increased to a maximum a few millimeters from the spinneret; this was followed by a monotonic decay. The maximum air velocity ($V_a^{\max}$) exceeded V_{a0}. For $V_{a0} = 30$ and 300 m/s, the $V_a^{\max}$ values were 33.4 and 420 m/s, respectively.

We determined analytical fit functions with the aid of the Origin 8.0 software (OriginLab Corp., Northampton, MA) for the axial $V_a(z)$ and $T_a(z)$ simulation data presented in ref. 21. The fit functions for $V_a(z)$ represented the velocity reduced by its maximum, $V_a(z)/V_a^{\max}$, versus the distance reduced by the width of the air slots (z/b). The variable z/b was divided into three ranges for $V_a(z)$ and two ranges for $T_a(z)$ to obtain the best fit to the simulation data by different fit functions in each range, with a continuous transition between the ranges. The velocity fit functions were parabolic within a very short range of the z axis of about $\frac{3}{4}\,b$ at the spinneret

$$\frac{V_a(z)}{V_a^{\max}} = 0.574\left(1.339\frac{z}{b} - 1\right)\frac{z}{b}, \quad 0 < \frac{z}{b} \le 0.747 \tag{18a}$$

followed by the sigmoid up to $z = z^*$

$$\frac{V_a(z)}{V_a^{\max}} = 1 - 3\left[1 + \exp\left(1.316\frac{z}{b} - 0.263\right)\right]^{-1}, \quad 0.747 < \frac{z}{b} \le \frac{z^*}{b} \tag{18b}$$

and by power-law decay above z^*

$$\frac{V_a(z)}{V_a^{\max}} = C\left(\frac{z}{b}\right)^{-0.572}, \frac{z}{b} > \frac{z^*}{b} \tag{18c}$$

where z^* was the axial distance of the intersection of the sigmoid with the decay plot. The axial distance from which V_a started decaying, reduced by the width of air slots, is given by the relation $z^*/b = C^{1.748}$, C is the fit coefficient and is calculated by $C = 3.310 + (3.949 \times 10^{-3})V_a^{\max}$, and $V_a^{\max}$ is expressed in meters/second. At high-velocity air jets ($V_a^{\max} > 200$ m/s), the coefficient C deviates considerably from a nearly fixed value at low velocity. In the literature, values of -0.610[34,35] and -0.632[8] of the power in eq. (18c) were obtained from experimental data, and a value of -0.568 was obtained from the simulation results[36] for air slots with a similar inclination angle of 30° to the z axis.

Two ranges of the axial distance were considered to fit the $T_a(z)$ simulation data presented in ref. 21. For the first range, we found

$$\frac{T_a(z) - T_{\text{amb}}}{T_{a0} - T_{\text{amb}}} = A + (1 - A)\left\{1 + \exp\left[0.714\left(\frac{z}{b} - x_0\right)\right]\right\}^{-1}, \; 0 < \frac{z}{b} \le \frac{z^*}{b} \tag{19a}$$

where $T_{a0} = 573$ K and $T_{\text{amb}} = 293$ K are the initial and ambient air temperatures, respectively; A and x_0 are fit coefficients: $A = 0.919 - 0.240\exp(-V_a^{\max}/70.21)$; $x_0 = 8.112 + 0.593\exp(V_a^{\max}/147.90)$; and $z^*/b = 8.818 + 0.434\exp(V_a^{\max}/168.70)$.

In the second range, the data fit the following power-law decay:

$$\frac{T_a(z) - T_{\text{amb}}}{T_{a0} - T_{\text{amb}}} = C\left(\frac{z}{b}\right)^{-0.590}, \; \frac{z}{b} > \frac{z^*}{b} \tag{19b}$$

where $C = 3.241 + (4.769 \times 10^{-3})V_a^{\max}$.

The $p_a(z)$ values simulated in ref. 21 showed a slight increase within a very short range of a few millimeters near the spinneret followed by fast decay to atmospheric pressure. Then, the influence of $p_a(z)$ on melt blowing was neglected.

The line plots in Figures 2 and 3 illustrate analytical fit to the simulation data[21] by eqs. (18a)–(18c), (19a), and (19b) for different V_{a0} values. A shifting of the plots for high-velocity air jets resulted from the dependence of C on $V_a^{\max}$. The simulation data and the fit functions are compared in Figure 2 with the experimental data (solid symbols) reported by Moore et al.[8] and Harpham and Shambaugh[35] for low ($V_{a0} = 17.3$ and 34.6 m/s[35]) and high ($V_{a0} = 352$ m/s[8])

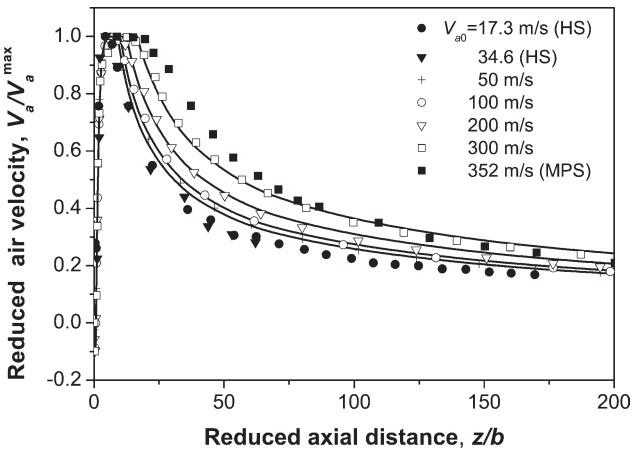

Figure 2 Reduced axial air velocity (V_a/V_a^{max}) versus reduced axial distance (z/b) at different V_{a0} values. Open symbols and crosses represent the simulation data,[21] Axial air temperature T_a presented as lines show the fit by eqs. (18a)–(18c), and solid symbols show the experimental data (HS = Harpham and Shambaugh;[35] MPS = Moore, Papavassiliou, and Shambaugh[8]).

V_{a0} values and the air slots with a similar inclination angle of 30°.

For $T_a(z)$, the simulation data and the fit functions are compared in Figure 3 with the experimental data for V_{a0} = 35 m/s and a T_{a0} of 300°C over the ambient temperature (solid symbols)[35] and with the power-law decay obtained in ref. 8 (dashed line) from experimental measurements for V_{a0} = 352 m/s and a T_{a0} of 300°C. The decay exponent, −0.590 in eq. (19b), was between the experimental values of −0.615[35] and −0.470.[8] The experimental data in Figures 2 and 3, rescaled for the axial variable z/b

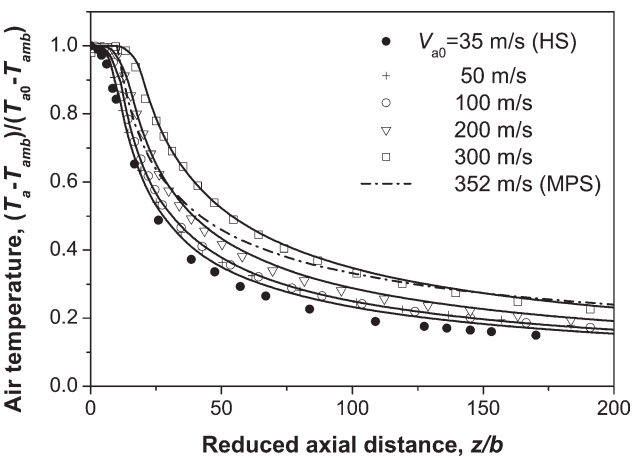

Figure 3 Axial air temperature T_a presented as $[(T_a - T_{amb})/(T_{a0} - T_{amb})]$ versus reduced distance (z/b) at different V_{a0} values. Open symbols and crosses show the simulation data,[21] solid lines show the fit by eqs. (19a) and (19b), solid symbols show the experimental data (HS = Harpham and Shambaugh[35]), and the dash-dotted line shows the experimental power-law decay (MPS = Moore, Papavassiliou, and Shambaugh[8]).

according to the geometry of the die assembly used in the experiments, provided satisfactory verification for the dependence of the simulation data and the fit functions on the axial variable and for the influence of V_{a0} on the $V_a(z)$ and $T_a(z)$ profiles.

RESULTS AND DISCUSSION

The online measurements and experimental observations[3,6,7] indicated that a majority of the filament attenuation occurred by air drawing within a short range of the process axis adjacent to the spinneret in which the polymer melt was subjected to extremely fast elongation. We use the presented model of melt air drawing to discuss the influence of $V_a(z)$, L, and the polymer molecular weight on the filament attenuation and dynamics of the melt blowing of iPP nonwovens. The range of the air-drawing zone in which $V_a(z)$ dominated local velocity of the filament, $V_a(z) > V(z)$, depended on the distribution of the axial velocity of the air jets and on the rheological response of the polymer. The stretching of the filaments due to interfilament collisions that contributed to some attenuation beyond the air-drawing zone was not considered. In our computations, we assumed that the initial temperatures of the melt and of the air were fixed at 300°C, the polymer W = 0.01 g/s, and the diameter of the spinneret orifice (D_0) was 0.35 mm.

Figure 4 shows the plots of the filament velocity at the collector (V_L) versus L computed for several M_w values between 100,000 and 300,000 and with the air jet with a fixed V_a^{max} of 300 m/s (solid lines). $V(z)$ is shown in the meters per minute unit widely used in melt spinning. For the collector located in the air-drawing zone, $V_a(z)$ (dashed line) dominated the velocity of the filament. The air-drawing model applies to processes with the collector location in the range of the z axis and is limited by the point at

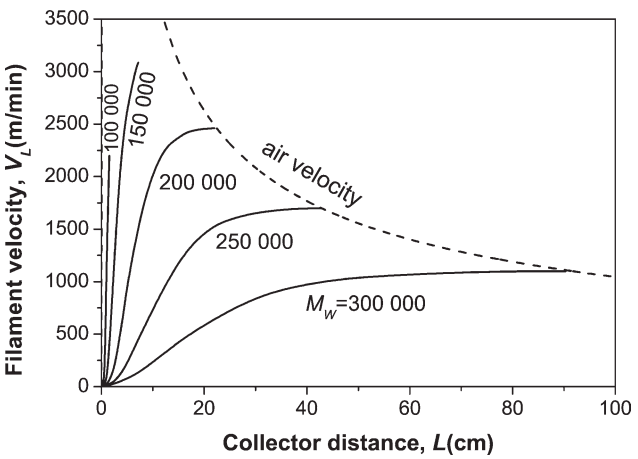

Figure 4 V_L of the iPP filament in the air-drawing zone versus L computed for different M_w's. The dashed line shows the centerline velocity of the air (V_a^{max} = 300 m/s).

TABLE I
M_w and η at 230 and 300°C Determined from Eq. (16) and Estimated MFR of iPP

M_w (Da)	η at 230°C (Pa s)	η at 300°C (Pa s)	MFR (g/10 min)
100,000	58	16	260
150,000	230	64	65
200,000	611	169	24
250,000	1305	360	12
300,000	2425	671	6

which $V(z)$ and $V_a(z)$ are equal. The length of the air-drawing zone considerably decreased with decreasing M_w, and the reduction was accompanied by increasing $V(z)$. Some velocity plots shown in Figure 4 discontinued for lower M_w before they achieved the edge of the air-drawing zone. The discontinuity was a consequence of a divergence of dV/dz in the computations. The divergence appeared closer to the spinneret for lower M_w and may have indicated an instability in the stationary process leading to the filament failure and different than the capillary wave instability.[14]

Table I indicates the relation between M_w and η at 300°C determined for iPP from eq. (16) and MFR determined from the formula MFR = Constant/(η at 230°C), where Constant = 1.5×10^4 Pa s and the shear viscosity is computed for 230°C.[32]

Figure 5 shows the $V(z)$ profiles computed from the model for several M_w values (solid lines) and the air-jet velocity with $V_a^{max} = 265$ m/s (dashed line) adjusted to the experimental data (crosses) published by Bresee and Ko[7] for the centerline $V_a(z)$. The solid symbols represent online experimental measurements of $V(z)$ versus distance from the spinneret in a process without the collector (infinite collector location) and $M_w = 63{,}000$ (MFR = 1259) from the literature.[7] The experimental data showed a maximum in the range where $V(z)$ approached the velocity of the air, which was similar to the simulation results obtained for different M_w values.

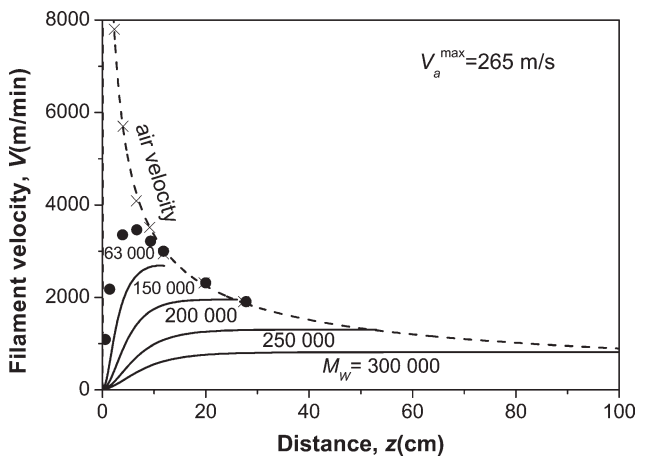

Figure 5 Filament velocity (V) versus z computed for different M_w's (solid lines) and $V_a^{max} = 265$ m/s (dashed line) adjusted to the experimental data (crosses).[7] Solid symbols show the experimental data[7] without the collector and $M_w = 63{,}000$ (MFR = 1259).

Figure 6 illustrates influence of $V_a(z)$ on V_L versus L (thick lines) predicted for several V_a^{max} values and $M_w = 250{,}000$. The thin-line plots show $V(z)$ profiles computed for the case of collector located at the air-drawing zone edge, and the dashed-line plots show the centerline velocity of the air beyond the zone.

In the processes with the collector located beyond the air-drawing zone, intensive coiling of the filaments took place because of a slowdown of the filaments by the decaying air jet beyond the zone. The coiling led to interfilament collisions, which resulted an in acceleration of some filaments and additional attenuation, broadening of the diameter distribution of the fibers, and more nonuniformities in the nonwovens. Online measurements of $V(z)$ by Bresee and Ko[7] indicated that the plots of the air and $V(z)$ values nearly overlapped beyond the air-drawing zone. Thus, we assumed that the filament axial velocity beyond the zone could be approximated by $V_a(z)$ given by eq. (18c), whereas, within the zone, it was approximated by the velocity computed for the case of the collector located at the zone edge. The approximation is illustrated in Figure 6 by connection of the thin- and dashed-line plots.

For the case of the collector position in the air-drawing zone, the $V(z)$ profiles should be located in Figure 6 between the thick-line plot of the velocity at the collector and the thin-line velocity profile determined for the case of the collector located at the zone edge. The highest $V(z)$ and attenuation were

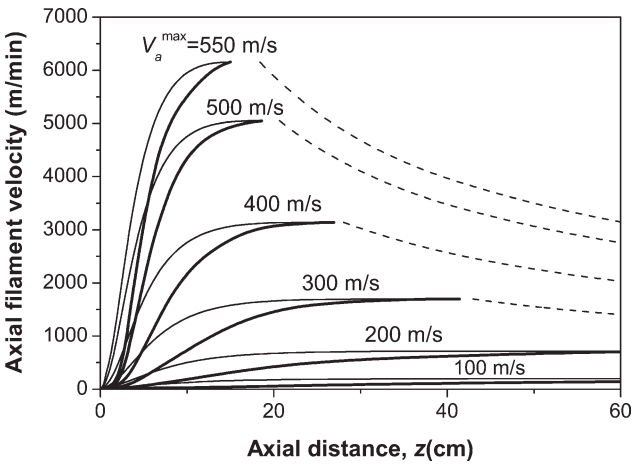

Figure 6 Axial velocity of the iPP filament versus z computed for different V_a^{max} values. Thick lines show the velocity at the collector, thin lines show the velocity profiles [$V(z)$] for the collector at the edge of the air-drawing zone, and dashed lines show the approximation beyond the air-drawing zone [eq. (18c); $M_w = 250{,}000$].

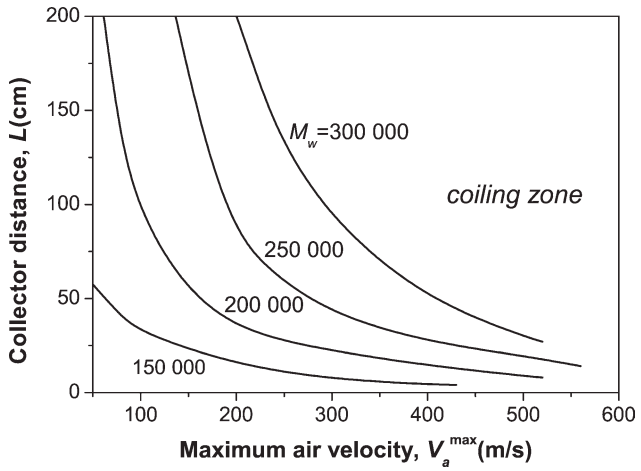

Figure 7 Ranges of the air-drawing zone in the space of maximum air-jet velocity (V_a^{max}) and L predicted for different M_w values of iPP.

predicted for the process with the collector location at the edge of the air-drawing zone, at which the most of the air-jet potential was used. Any shift of the collector from the edge position toward the die reduced the efficiency of the air jet. Figures 4 and 6 indicate also that the air-drawing zone was shorter for faster air jets and lower molecular weights.

Figure 7 shows a diagram in the space of V_a^{max} versus L, which indicates the length of the air-drawing zone for several M_w values. The zone decreased to a few centimeters at high V_a^{max} and low M_w values. The discontinuity of the $V(z)$ plots in the air-drawing zone associated with a divergence of the melt dV/dz in the computations is also shown in Figures 6 and 7 for high-velocity jets. This may indicate an instability of the flow deformation in the process at such collector locations. The discontinuity appeared closer to the spinneret for faster air-jet velocities. The fastest air jet assured convergent computations, and therefore, the prediction of stationary air drawing was found for $V_a^{max} = 565$ m/s and $M_w = 250{,}000$.

The influence of the air-jet velocity on the filament diameter at the collector (D_L) versus L is illustrated in Figure 8 for several V_a^{max} values between 100 and 550 m/s and for $M_w = 250{,}000$. The solid-line plots show the results obtained for the collector located in the air-drawing zone, whereas the dashed-line plots are the predicted values for the collector beyond the zone with an assumption that the interfilament collisions contributed to the filament attenuation negligibly. Any downstream shift of the collector from any point in the air-drawing zone led to finer fibers, until the zone edge, where the air-jet potential was exhausted. Further attenuation, although less effective, may have occurred by stochastic interfilament collisions not considered in this model. We predicted that with increasing V_a^{max} to 550 m/s, $D(z)$ decreased in the process to about 12 μm and attenuation occurred within a very short range of about 6 cm, in which the polymer accelerated to about 6000 m/min.

The model predictions for the $D(z)$ profile along the process axis are compared in Figure 9 (line plots) with experimental data from the literature (points) as reported by Bansal and Shambaugh[3] for low V_a^{max} values and Bresee and Ko[7] for high V_a^{max} values. iPP with $M_w = 122{,}500$ and hot air (300°C) with a V_{a0} of 51.4 m/s were used in ref. 3. $V_a^{max} = 59.6$ m/s was assumed in the computations; this value was 16% higher than V_{a0}, as we estimated on the basis of the simulation data[21] for this range of air-jet velocities and similar geometry of the die assembly. The measured diameter (circles) and the values computed for the same processing and material parameters as in the experiment (solid line) remained in a good agreement in the range of fast attenuation near the die and in the far-distance range, with some discrepancy between. Similar agreement is shown in the figure for high-velocity air jets, where the experimental data (squares) and the diameter profile computed at $V_a^{max} = 265$ m/s and $M_w = 63{,}000$ (MFR = 1259) (dashed line) showed considerably lower values.

The minimum $D(z)$ attainable by the adjustment of the collector position to the edge of the air-drawing zone is plotted versus V_a^{max} in Figure 10 for several M_w values. We predicted that any reduction in M_w would lead to finer filaments in the entire range of V_a^{max}.

Figures 11 and 12 show dV/dz and $T(z)$ versus distance z for several V_a^{max} values and $M_w = 250{,}000$ computed for the collector at the edge of the air-drawing zone. The maximum dV/dz was located near the spinneret, shifted slightly upstream with increasing $V_a(z)$, and approached a high value of

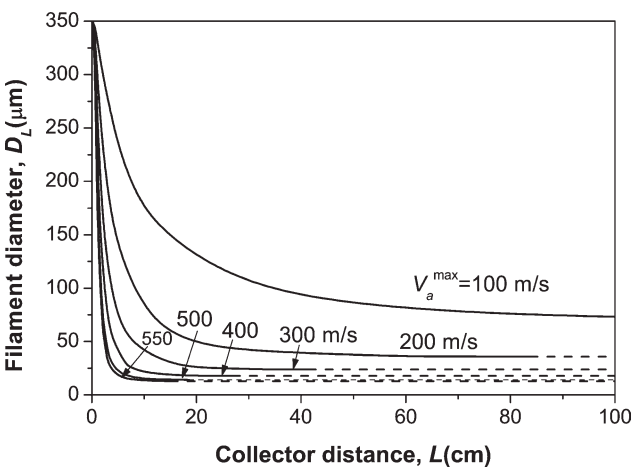

Figure 8 D_L versus L predicted for iPP at different V_a^{max} values. Solid lines show the collector in the air-drawing zone, and dashed lines show the approximation for the collector beyond the zone ($M_w = 250{,}000$).

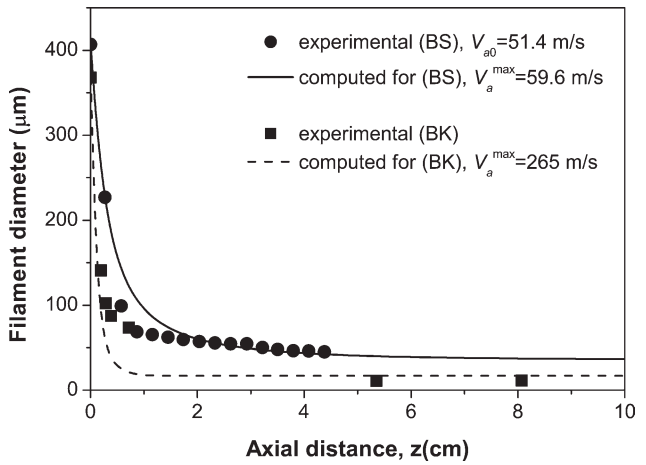

Figure 9 $D(z)$ versus z. Symbols show the experimental data reported by Bansal and Shambaugh (BS)[3] and Bresee and Ko (BK).[7] Line plots show the values computed from the model for processing and material parameters used in the experiments.

about 1900 s^{-1} at $V_a^{max} = 550$ m/s. Although the value exceeded several times the dV/dz values in high-speed melt spinning,[37,38] the final $V(z)$ values attainable in both processes were comparable. A second local maximum of dV/dz of about 1300 s^{-1}, at a distance closer to the spinneret was also predicted for the highest V_a^{max}.

The local temperature of the filament exceeded the equilibrium melting point ($T_m^0 = 453$ K) of iPP[14] in the entire air-drawing zone for $V_a^{max} > 400$ m/s and less than 20 cm from the spinneret for all considered V_a^{max} values. For processes with the collector beyond the air-drawing zone, we approximated $T(z)$ outside the zone, before the filament approached the collector, by the polymer temperature at the zone edge because α^* outside the zone decreased to zero ($\alpha^* \rightarrow 0$) because of the reduction of Re. With this approximation, the temperature profiles in Figure 12 were completed by the dashed-line plots, which represent the nearly constant temperature of the filaments after they left the air-drawing zone. We expect that the approximation should be better for faster air jets and for the collector locations closer to the zone. In reality, the temperature profiles should be smoother at the transition over the zone edge than those shown in Figure 12 because of cooling by radiation and convection at increasing stochastic motion of the filaments.

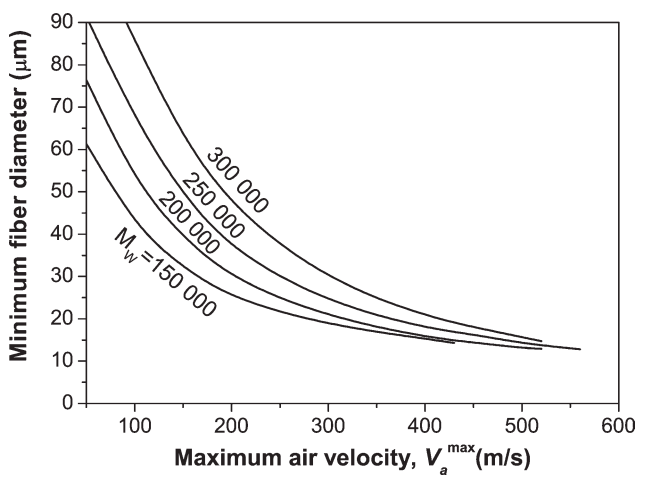

Figure 10 Minimum $D(z)$ versus maximum air-jet velocity (V_a^{max}) computed for different M_w values of iPP and the collector located at the edge of the air-drawing zone.

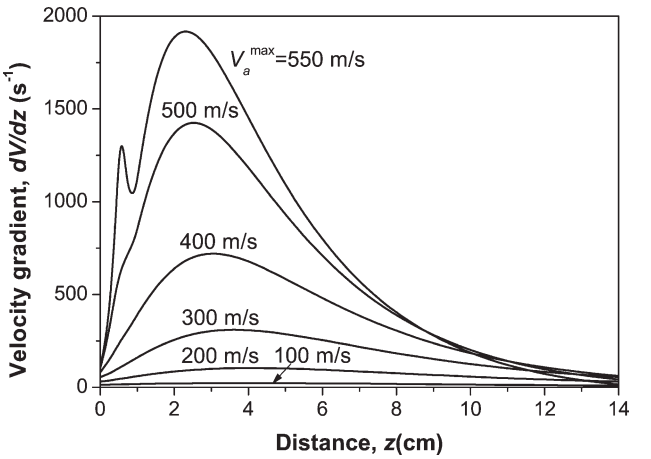

Figure 11 dV/dz of the iPP filament versus z computed for different V_a^{max} values and the collector located at the edge of the air-drawing zone ($M_w = 250{,}000$).

Figure 13 shows the average Δp over the filament cross section versus distance z for the collector located at the edge of the air-drawing zone at different V_a^{max} values and $M_w = 250{,}000$. Unlike in melt spinning, Δp was predicted to concentrate near the spinneret. Although the maximum $F(z)$ was found at the initial point, $z = 0$, the initial Δp was very low

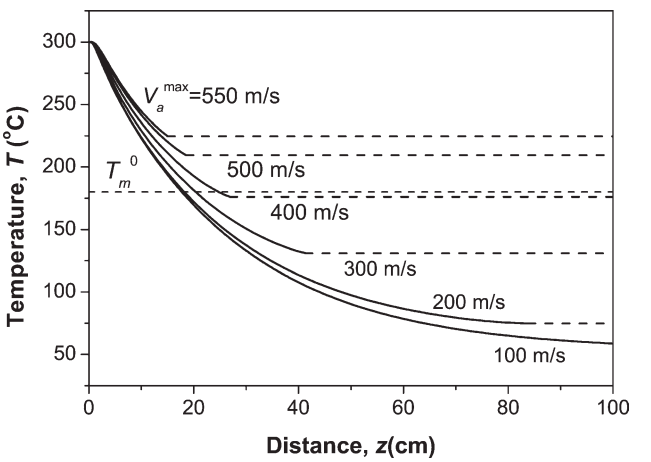

Figure 12 Local temperature of the iPP filament (T) versus z computed for different V_a^{max} values. Solid lines show the collector at the edge of the air-drawing zone, and dashed lines show the collector beyond the zone (approximation; $M_w = 250{,}000$).

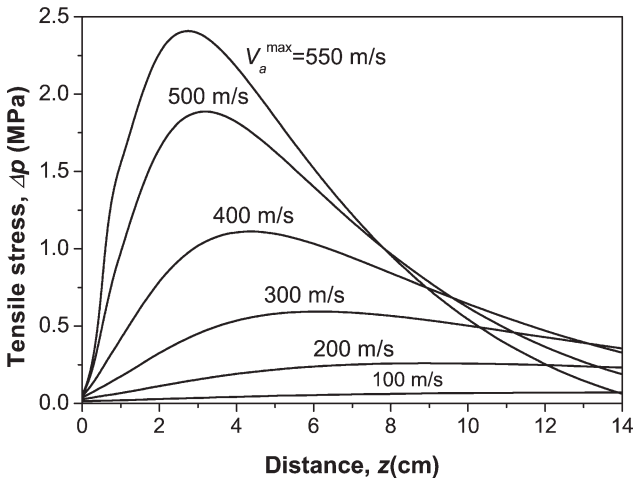

Figure 13 Local Δp of the iPP filament versus z computed for different V_a^{max} values and the collector at the edge of the air-drawing zone ($M_w = 250{,}000$).

and steeply increased to a maximum a short distance from the spinneret because of the rapid attenuation of the filament. The Δp maximum increased with increasing V_a^{max} and shifted upstream to about 3 cm from the spinneret for $V_a^{max} = 550$ m/s. The ranges of high Δp and high dV/dz on the z axis coincide in Figure 11, with a slight downstream shift of the stresses because of higher melt viscosity at lower temperatures. Despite dV/dz values several times higher than those in high-speed melt spinning, the maximum Δp values predicted in the computations were lower.[17,39]

The temperature and Δp profiles in Figures 12 and 13 indicate that the filaments should not have crystallized before they approached the collector. In the range of high Δp values, the polymer temperature was above T_m^0. When the filament cooled down below T_m^0 further on the z axis, it should not have crystallize by stress-induced crystallization before approaching the collector because the stress relaxed nearly to zero in that range and the polymer residence time was too short for crystallization. The minimum crystallization half period of unoriented iPP is about 1.25 s,[14] whereas the residence time on the z axis is shorter by two orders of magnitude. The spherulitic structure of iPP filaments observed in melt-blown nonwovens[7] indicated that crystallization occurred under relaxed molecular orientation during the cooling of the web on the collector.

Unlike in melt spinning, the inertia and air drag forces are opposite in melt blowing and compensate each other to a large extent, in particular, in the range of high dV/dz values. Under such conditions, low-level forces, such as surface tension, are expected to influence the process dynamics to a higher extent than in melt spinning. The surface tension (γ) contributes a positive gradient to the filament tension in eq. (2) and should enhance air drawing. Its contribution to the filament tension associated with a reduction of the diameter in the attenuation by ΔD over a range Δz of the process axis was $\pi\gamma\Delta D$, at a nearly constant γ in this range. For air jets with $V_a^{max} = 550$ m/s, the collector located at the edge of the air-drawing zone, and $M_w = 250{,}000$, the highest dV/dz was about 1900 s^{-1} at a distance of about 2.5 cm from the die and the highest dD/dz of about 10^3 μm/cm of the process axis was predicted a few millimeters from the die.

For this process, the surface tension term in eq. (2) was one order of magnitude higher than the gravity term in the range between the die and the maximum of the dV/dz. Analysis indicated that the surface tension shifted the point at which $D(z)$ decreased to 10% of its initial value from a distance of 2.03 to 1.45 cm toward the die in this process. The influence of the surface tension on $D(z)$ can be neglected for processes with a maximum dV/dz below 1400 s^{-1}. The surface tension forces should be also considered in an analysis of the limitations observed in melt blowing of superthin fibers;[40] a more detailed analysis of all dynamic contributions will come in a separate work.

The computations indicated that the viscous friction heat term in eq. (3) elevated $T(z)$, in particular, at higher air-jet velocities. In the process with $V_a^{max} = 550$ m/s, $M_w = 250{,}000$, and the collector at the air-drawing zone edge, $T(z)$ was elevated by about 1.5°C at the maximum dV/dz, up to by about 18°C at the $L = 8.6$ cm. Such an increase in $T(z)$ enhanced the melt processability by increasing its fluidity and allowed for higher attenuation, from 24.6 to 14.1 μm at the zone edge in this process. The viscous friction heat may have contributed to the plateaulike behavior of $T(z)$ observed experimentally at distances above 4–5 cm from the die by Shambaugh and coworkers.[3,41]

The model predicted negative p_{rh} in the polymer bulk created during fast elongation of the viscoelastic melt under high-velocity air jets in the supersonic range. Axial profiles of p_{rh} are plotted in Figure 14 for different V_a^{max} values with $M_w = 250{,}000$ and with the collector located at the edge of the air-drawing zone. The pressure was created with the filament very close to the spinneret in a narrow range of the process axis of about 1–2 cm. Its location coincided with the secondary maximum of dV/dz presented in Figure 11 for the fastest air jet. The negative p_{rh} acted against the cohesion forces, and when the stress level approached a cohesion limit, it may have been released by cavitation in the polymer bulk. p_{rh} disappears for a purely viscous fluid subjected to the process.

Figure 15 shows the maximum of $|p_{rh}|$ plotted versus L for different V_a^{max} values and with $M_w =$

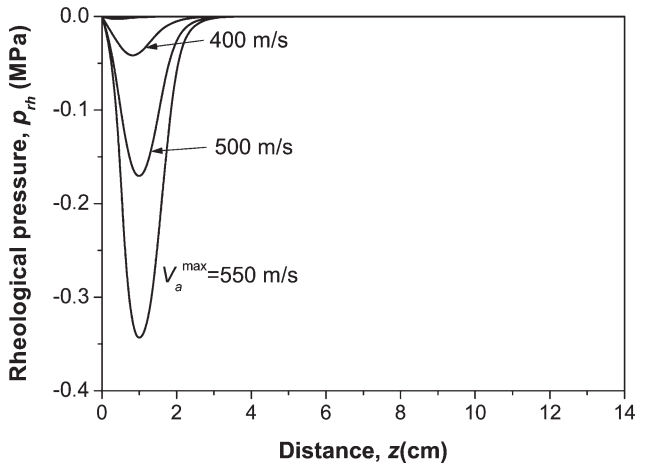

Figure 14 p_{rh} in the iPP filament versus z computed for different V_a^{max} values and the collector at the edge of the air-drawing zone ($M_w = 250{,}000$).

250,000. The values and positions of the maximum on the z axis were almost insensitive to L for $L > 6$ cm, whereas at closer collector locations, they decreased to zero when the collector was shifted upstream. The dashed-line plots show approximations for the collector outside the air-drawing zone by the values obtained for the collector at the zone edge. Figure 16 illustrates the nearly logarithmic increase of the maximum of the $|p_{rh}|$ with increasing V_a^{max} in the supersonic range for different M_w values, with the highest value of about 0.4 MPa at $V_a^{max} = 565$ m/s and $M_w = 250{,}000$.

A high negative p_{rh} acting against the cohesion forces could provide enough potential energy for cavitation in the polymer bulk and longitudinal splitting of the filament into subfilaments. Assuming that potential energy of p_{rh} was converted into the surface energy of n subfilaments produced in the spitting, we considered the following energy balance equation:

$$p_{rh}\delta v + \sigma\left[\sum_{i=1}^{n}\delta s_i - \delta s_D\right] = 0 \qquad (20)$$

where σ is the surface free energy density of the polymer, δ_S is the surface of the i-the subfilament, and the sum represents surface of the subfilaments created by the splitting of a filament section of volume δv and surface δs_D. Equation (20) is based on the assumption that the potential energy associated with the release of p_{rh} during the splitting from p_{rh} to a residual extrapressure p_{rel} remaining in the subfilaments after the splitting in δv $[(p_{rel} - p_{rh})\delta v]$ converts in total to the surface energy of n subfilaments:

$$\sigma\left[\sum_{i=1}^{n}\delta s_i - \delta s_D\right]$$

At the full pressure release to $p_{rel} = 0$, we obtain eq. (20).

For the splitting of the filament at a point z of the process axis, involving a filament section of local $D(z)$ and length δl and creating n identical cylindrical subfilaments of diameter d, eq. (20) and the mass conservation equation $n\pi\rho(z)d^2\delta l/4 = \pi\rho(z)D^2(z)\delta l/4$ lead to the following formula for the hypothetical split diameter (d):

$$\frac{1}{d(z)} = \frac{1}{D(z)} - \frac{p_{rh}(z)}{4\sigma(z)} \qquad (21)$$

where $\sigma(z)$ is the local surface free energy density at $T(z)$. These computations indicate that iPP filaments do not solidify in the air-drawing zone, and the

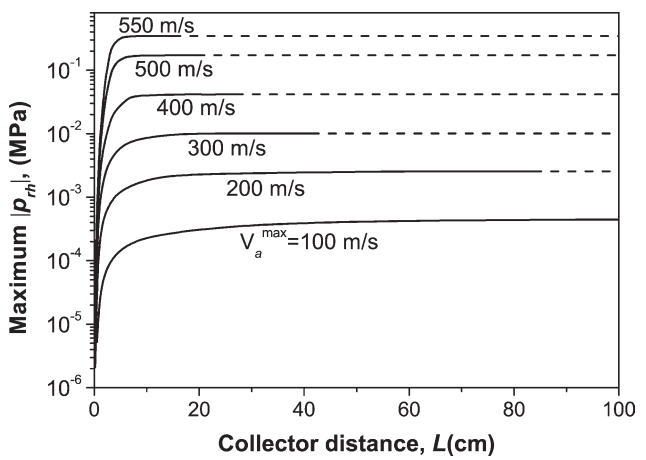

Figure 15 Maximum $|p_{rh}|$ in the iPP filament versus L for different V_a^{max} values. Solid lines show the collector in the air-drawing zone, and dashed lines show the collector beyond the zone (approximation; $M_w = 250{,}000$).

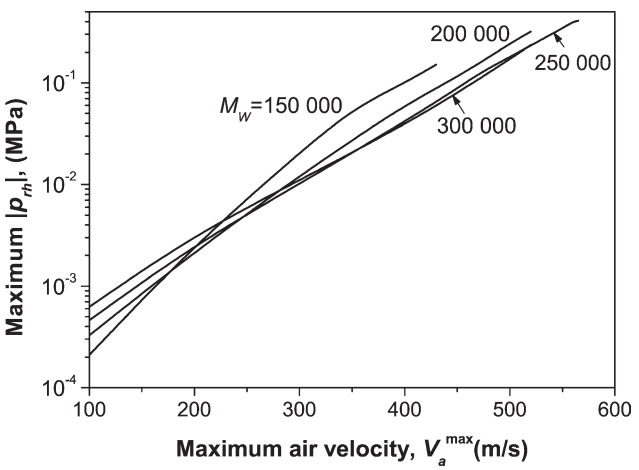

Figure 16 Maximum $|p_{rh}|$ in the iPP filament versus V_a^{max} for different M_w values and the collector at the edge of the air-drawing zone.

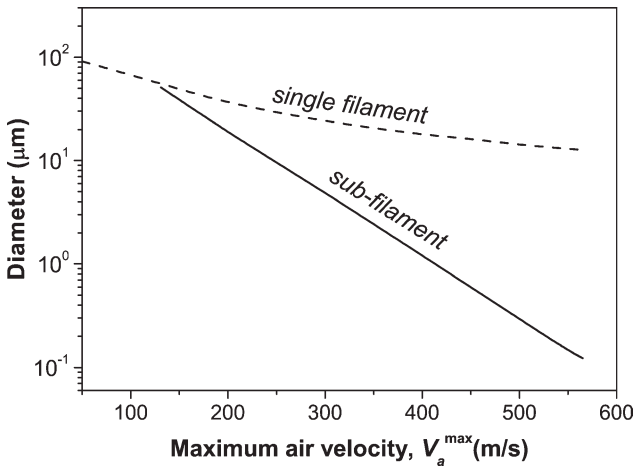

Figure 17 Diameter of the iPP subfilaments (solid line) in the hypothetical pressure-induced splitting of the filament and $D(z)$ without splitting (dashed line) versus V_a^{max} predicted for the collector at the edge of the air-drawing zone ($M_w = 250{,}000$).

temperature dependence of the surface free energy is given by eq. (9). For high negative p_{rh} [$-p_{rh}(z) \gg 4\sigma(z)/D(z)$], we have $d(z) \cong -4\sigma(z)/p_{rh}(z)$.

Figure 17 shows d plotted versus V_a^{max} (solid line) predicted from eq. (21) for the maximum $|p_{rh}|$, with the collector location at the edge of the air-drawing zone and $M_w = 250{,}000$. The dashed-line plot illustrates $D(z)$ at the collector without splitting. We predicted that, in the range of supersonic air jets, the postulated pressure-induced splitting should reduce $D(z)$ by two orders of magnitude to the bottom of the range of superthin fibers, that is, to about 0.1 μm at $V_a^{max} = 550$ m/s. Further attenuation of the subfilaments by air drawing after the splitting was not considered in this study.

Burst splitting of polypropylene monofilaments induced by inside pressure was shown by Gerking[42] in a photo of a filament subjected to supersonic air jet in a Laval nozzle. It was reported that up to several hundred subfilaments were created from a single filament by longitudinal bursting under such conditions.[42]

CONCLUSIONS

A single-filament model of stationary air drawing in the melt blowing of nonwovens with predetermined $V_a(z)$ and $T_a(z)$ fields, which accounted for melt viscoelasticity, viscous friction heat in the filament bulk, and surface energy, allowed us to discuss the dynamics of the process and to determine axial profiles of $V(z)$, dV/dz, $T(z)$, $D(z)$, $\Delta p(z)$, and $p_{rh}(z)$. Example computations performed for iPP melt blowing indicated a significant influence of the air-jet velocity, L, and polymer molecular weight (MFR) on the filament attenuation and process dynamics.

The air-drawing zone was sensitive to the air-jet velocity and the polymer M_w. The zone was shorter for faster air jets and lower M_w and decreased to a few centimeters for supersonic air jets and low M_w's (high MFRs). The reduction was accompanied by a considerable increase in filament dV/dz, attenuation, and velocity. Any downstream shift of the collector in the air-drawing zone led to a higher lay-down velocity of the filaments on the collector and finer fibers until the zone edge, at which the air-jet potential was exhausted and the highest attenuation by air drawing was predicted. A reduction in M_w led to a faster lay down and finer filaments in the entire range of $V_a(z)$ and the die-to-collector locations in the air-drawing zone.

In the case of collector locations beyond the zone, further filament attenuation occurred, although it was much less effective, as a consequence of interfilament collisions. An approximation of the axial $V(z)$ was proposed for processes with the collector located outside the air-drawing zone: within the air-drawing zone, $V(z)$ was approximated by the velocity computed for the collector at the zone edge, and beyond that zone, $V(z)$ was approximated by $V_a(z)$ along the centerline of the jets.

The Δp and dV/dz maxima were predicted to be located near the spinneret, with an upstream shift at increasing air-jet velocity. Δp was very low at the spinneret and steeply increased to a maximum despite a monotonic decrease in $F(z)$ from its maximum at the spinneret. The maximum of Δp was higher for faster air jets and shifted upstream to the spinneret. The melt dV/dz values predicted for fast air jets exceeded by several times the values reported for high-speed melt spinning, although the Δp values in air drawing were significantly lower, and the $V(z)$ values attainable in both processes were similar.

Axial profiles of $T(z)$ and Δp indicated that the polymer should not have crystallized in the melt blowing of nonwovens before the filament approached the collector and that the melt bonding of the filaments should occur on the collector during the cooling of the web.

Considerable negative p_{rh} was predicted in the polymer bulk as a result of the viscoelasticity of the melt being subjected to fast uniaxial elongation in supersonic air jets. The range of the creation of p_{rh} on the process axis was very narrow and was located near the spinneret. The maximum and position of the absolute value of the pressure on the axis were insensitive to the collector locations above 6 cm from the spinneret. The negative p_{rh} acted against the cohesion forces in the polymer melt and may have created cavitation and induced the burst splitting of the air-drawn filament into subfilaments. A hypothetical average split diameter was inversely proportional to the maximum of the absolute value

of the pressure. A nearly logarithmic increase of the maximum was predicted with increasing air-jet velocity in the supersonic range. The postulated pressure-induced splitting could reduce $D(z)$ well down to the range of superthin fibers.

References

1. Buntin, R. R.; Keller, J. P.; Harding, J. W. U.S. Pat. 3,849,241 (1974).
2. Harding, J. W.; Keller, J. P.; Buntin, R. R. U.S. Pat. 3,825,380 (1974).
3. Bansal, V.; Shambaugh, R. L. Ind Eng Chem Res 1998, 37, 1799.
4. McCulloch, J. G. Int Nonwovens J 1999, 8 (Spring), 66.
5. Zhang, D.; Sun, C.; Wadsworth, L. C. Text Res J 2001, 71, 301.
6. Farer, R.; Batra, S. K.; Ghosh, T. K.; Grant, E.; Seyam, A. M. Int Nonwovens J 2003, 12 (Spring), 36.
7. Bresee, R. R.; Ko, W. C. Int Nonwovens J 2003, 12 (Summer), 21.
8. Moore, E. M.; Papavassiliou, D. V.; Shambaugh, R. L. Int Nonwovens J 2004, 13 (Fall), 43.
9. Chen, T.; Huang, X. Text Res J 2003, 73, 651.
10. Chen, T.; Wang, X.; Huang, X. Text Res J 2004, 74, 1018.
11. Andrews, E. H. Brit J Appl Phys 1959, 10, 39.
12. Ziabicki, A.; Kędzierska, K. Kolloid Z 1960, 171, 51.
13. (a) Ziabicki, A. Kolloid Z 1961, 175, 14; (b) Ziabicki, A. Kolloid Z 1961, 179, 116.
14. Ziabicki, A. Fundamentals of Fibre Formation; Wiley: London, 1976.
15. Kase, S.; Matsuo, T. J Polym Sci Part A: Gen Pap 1965, 3, 2541.
16. Kase, S.; Matsuo, T. J Appl Polym Sci 1967, 11, 251.
17. Ziabicki, A.; Jarecki, L.; Wasiak, A. Comput Theor Polym Sci 1998, 8, 143.
18. Petrie, C. J. S. Elongational Flows; Pitman: London, 1979.
19. Pope, S. B. Turbulent Flows; Cambridge University Press: Cambridge, 2000; p 134.
20. Krutka, H. M.; Shambaugh, R. L.; Papavassiliou, D. V. Ind Eng Chem Res 2003, 42, 5541.
21. Zachara, A.; Lewandowski, Z. Fibers Text Eastern Eur 2008, 16, 17.
22. Lewandowski, Z.; Ziabicki, A.; Jarecki, L. Fibres Text Eastern Eur 2007, 15, 77.
23. Jarecki, L.; Ziabicki, A. Fibres Text Eastern Eur 2008, 16, 17.
24. Jarecki, L.; Lewandowski, Z. Text Eastern Eur 2009, 17, 75.
25. Matsui, M. Trans Soc Rheol 1976, 20, 465.
26. Majumdar, B.; Shambaugh, R. L. J Rheol 1990, 34, 591.
27. Zieminski, K. F.; Spruiell, J. E. Synth Fibers 1986, 4, 31.
28. Mark, J. E. Physical Properties of Polymers Handbook; AIP: New York, 1996; pp 424, 670.
29. Phan-Thien, N. J Rheol 1978, 22, 259.
30. Larson, R. G. Constitutive Equations for Polymer Melts and Solutions; Butterworth: Boston, 1988; p 171.
31. Lee, J. S.; Shin, D. M.; Jung, H. W.; Hyun, J. C. J Non-Newtonian Fluid Mech 2005, 130, 110.
32. van Krevelen, D. W. Properties of Polymers; Elsevier: Amsterdam, 2000; pp 86, 463, 469, 676.
33. Rao, R. S.; Shambaugh, R. L. Ind Eng Chem Res 1993, 32, 3100.
34. Krutka, M. H.; Shambaugh, R. L.; Papavassiliou, D. V. Ind Eng Chem Res 2002, 41, 5125.
35. Harpham, A. S.; Shambaugh, R. L. Ind Eng Chem Res 1996, 35, 3776.
36. Krutka, H. M.; Shambaugh, R. L.; Papavassiliou, D. V. Int Nonwovens J 2005, 14 (Spring), 2.
37. Ziabicki, A.; Kawai, H. High-Speed Fiber Spinning; Wiley: New York, 1976.
38. Jarecki, L. In Progress in Understanding of Polymer Crystallization; Reiter, G.; Strobl, G. R., Eds.; Springer-Verlag: Berlin, 2007; p 65.
39. Jarecki, L.; Ziabicki, A.; Blim, A. Comput Theor Polym Sci 2000, 10, 63.
40. Ellison, C. J.; Phatac, A.; Giles, D. W.; Macosco, C. W.; Bates, F. S. Polymer 2007, 48, 3306.
41. Marla, V. T.; Shambaugh, R. L.; Papavassiliou, D. V. Ind Eng Chem Res 2009, 48, 8736.
42. (a) Gerking, L. Chem Fibers Int 2002, 52, 424; (b) Gerking, L. Chem Fibers Int 2004, 54, 261; (c) Gerking, L. Chem Fibers Int 2005, 55, 52.